Nano Energy 55 (2019) 526–533

Contents lists available at ScienceDirect

Nano Energy

journal homepage: www.elsevier.com/locate/nanoen

Full paper

Novel $NaTi_2(PO_4)_3$ nanowire clusters as high performance cathodes for Mg-Na hybrid-ion batteries

Yanan Xu, Weijie Cao, Yameng Yin, Jinzhi Sheng, Qinyou An*, Qiulong Wei, Wei Yang, Liqiang Mai*

State Key Laboratory of Advanced Technology for Materials Synthesis and Processing, International School of Materials Science and Engineering, Wuhan University of Technology, Hubei, Wuhan 430070, PR China

ARTICLE INFO

Keywords:
Mg-Na hybrid-ion batteries
$NaTi_2(PO_4)_3$
NASICON
Nanowire clusters
High performance

ABSTRACT

Magnesium ion batteries (MIBs) are promising for large-scale energy storage but limited by the poor diffusion kinetics of the cathodes. Hybrid ion batteries, which combine both the advantages of fast alkali metal ions intercalation cathode and dendrite-free Mg anode that exhibits satisfactory electrochemical performance, are an option. Herein, a novel $NaTi_2(PO_4)_3$ nanowire clusters (NTP-NW/C) as hybrid magnesium-sodium ion batteries (MSIBs) cathode is presented for the first time. Combining the advantages of NTP nanowires and the homogeneous carbon skeleton, the novel 3D hierarchical structure endows short ion transport pathway, fast charge transfer speed and robust structure stability during sodiation/de-sodiation. As a result, the hybrid MSIB showed good electrochemical performances: a high reversible capacity of 124 mA h g^{-1} at 1 C, good rate capability (60 mA h g^{-1} at 10 C) and cycling stability (capacity retention of 97% after 100 cycles at 5 C). This novel design will be highly promising for large-scale energy storage applications.

1. Introduction

Magnesium-ion batteries (MIBs) as a substitute to lithium-ion batteries (LIBs) have showed great advantage to be the next generation electrochemical energy storage technology [1–4]. Compared with lithium, magnesium resources are abundant, distributed evenly as well as easy to be mined on earth, which shows inherent cost advantage [5,6]. Due to the divalent property of Mg^{2+}, magnesium possesses a higher volumetric capacity of 3833 m A h cm^{-3} compared with that of lithium (2046 m A h cm^{-3}) [6]. Most importantly, unlike lithium and sodium metal anodes, magnesium metal can be safely handled in ambient environment, and is dendrite-free growth on deposition, suggesting higher security in practical application [7,8]. However, the challenge for searching suitable cathodes need to be addressed before realizing the full potential of Mg batteries. Apart from the low potential Chevrel phase materials (1.1 V vs Mg/Mg^{2+}) [9], higher reversible Mg intercalation materials remain undetected. This is because that the strong interaction between Mg^{2+} and the host lattice results in sluggish solid-state diffusion and large potential polarization [10–12]. Recently, Nazar's group reported thiospinel TiS_2 as a high reversible Mg battery cathode with a high specific capacity of 190 mA h g^{-1}, however, this system only can be worked at an elevated temperature of 60 °C, which is detrimental to the practical application [13]. Thus, the fact of lacking suitable intercalation cathode materials is still a big bottleneck faced in this field.

Taking all these into considerations, to fully exert the advantages of both cathode and anode, hybrid ion batteries are a promising option [14,15]. Magnesium–lithium hybrid ion batteries (MLIBs) have been demonstrated one promising energy storage technology, which combines the benefits of fast and highly reversible Li-insertion cathode and high-capacity Mg anode that exhibits satisfactory cycling stability [15–19]. However, as analogues of rechargeable MLIBs, the study of low cost magnesium–sodium hybrid ion batteries (MSIBs) is very limited. This may be due to the higher requirements for the electrolyte systems. Similar to that of MLIBs, the operating mechanism for one MSIB is shown in Fig. 1a: the electrolyte comprises the common MIB electrolyte and the addition of suitable Na salt to form the dual salt electrolytes. During the discharge, Mg metal is dissolved in electrolyte to form $[Mg_2Cl_2]^{2+}$ dimer cations. Meanwhile, Na^+ ions are insertion into the cathode, and electrons are transferred through the external circuit from the Mg anode to the cathode to maintain the whole electrical neutrality. During the charge, Na^+ ions are deintercalated from the cathode into electrolyte, and the $[Mg_2Cl_2]^{2+}$ cations are deposited as Mg on the anode. Due to the higher redox potential of Mg^{2+}/Mg,

* Corresponding authors.
E-mail addresses: anqinyou86@whut.edu.cn (Q. An), mlq518@whut.edu.cn (L. Mai).

https://doi.org/10.1016/j.nanoen.2018.10.064
Received 30 September 2018; Received in revised form 25 October 2018; Accepted 29 October 2018
Available online 30 October 2018

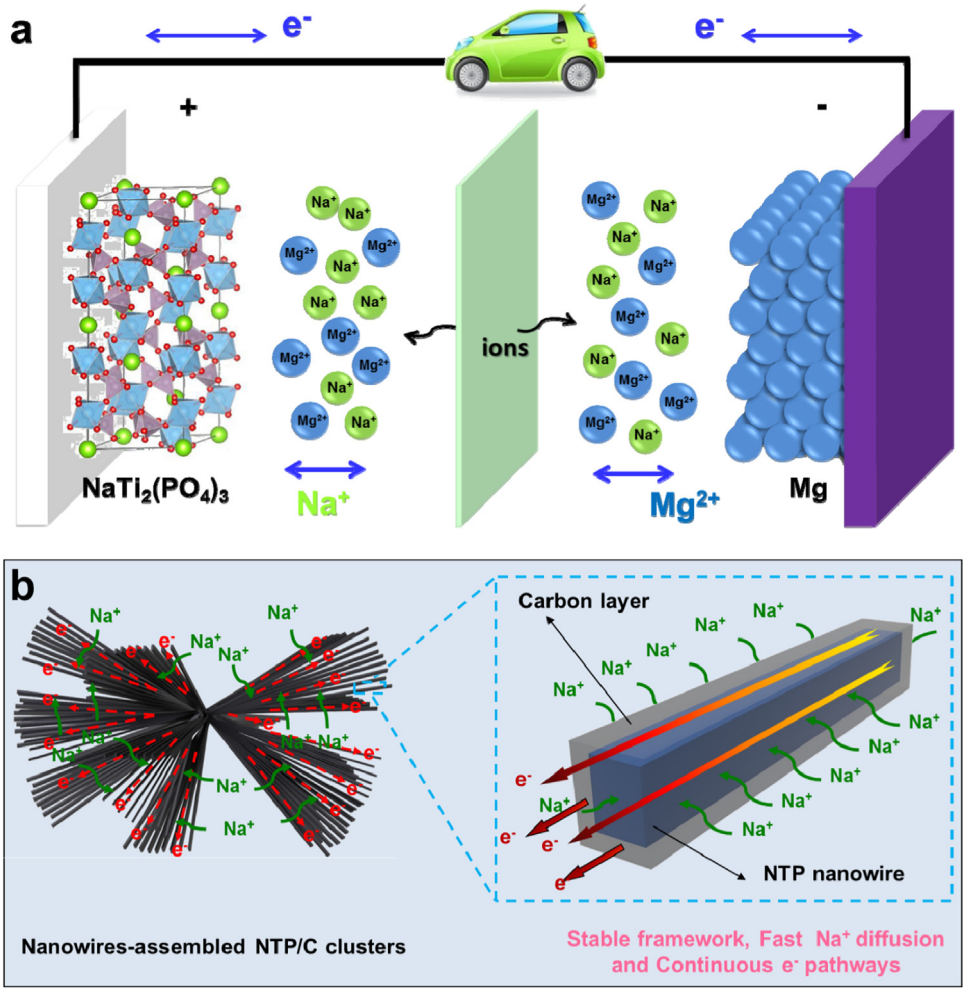

Fig. 1. (a) Schematic illustration of the Mg-Na hybrid battery designed in this work. (b) Schematic illustration of carbon-coated hierarchical NTP-NW/C nanowire clusters with stable framework, fast Na^+ diffusion and continuous e^- pathways.

Mg^{2+} ions are favored to be deposited/dissolved at the anode than that of Na^+. But it should be noted that the matching of dual salt electrolytes with the cathode is the key point when designing a MSIB. So far, the available dual salt electrolytes contain $NaBH_4$ + $Mg(BH_4)_2$ in diglyme [10] and $[Mg_2(m\text{-}Cl)_2][AlCl_4]_2$ + $NaAlCl_4$ in dimethoxythane (DME) [12,20]. But both the above electrolytes possess low cut-off upper voltage ($\leq$3.0 V *vs* Mg/Mg^{2+}). Besides, to avoid the side reactions between common noninert metal current collectors and electrolytes, the upper voltage must be under 2.0 V (*vs* Mg/Mg^{2+}) [10]. Therefore, the option of cathode materials should match the stability window of the electrolyte especially using low cost stainless steel as current collector. Recently, NASICON structured $NaTi_2(PO_4)_3$ (NTP) is regarded as a promising electrode of SIB with high Na^+ conductivity, low cost, and environmental compatibility [21–25]. Due to the proper potential of 1.7 V (*vs* Mg/Mg^{2+}), as the cathode for magnesium–sodium hybrid ion batteries, the NTP will show great application potential.

Herein, we report a high performance MSIB with NASICON-type NTP as the cathode, dendrite-free Mg metal as the anode, $[Mg_2(m\text{-}Cl)_2][AlCl_4]_2$ + $NaAlCl_4$ in DME as the electrolyte. A novel $NaTi_2(PO_4)_3$ microstructure composed of self-assembled carbon-coated nanowires (denoted as NTP-NW/C) is first reported. The as-prepared hierarchical structures not only inherit the superior characteristics of the 1D nanowires but also gain additional benefits from the unique secondary architectures (Fig. 1b): (1) the open structure of the self-assembled $NaTi_2(PO_4)_3$ nanoarchitecture would facilitate electrolyte penetration; (2) uniform distribution nanowires provide sufficient active sites and endow facile ion transport; (3) the carbon skeleton guarantees rapid and continuous electron transfer as well as improved structural stability. As a result, the novel NTP-NW/C electrodes exhibit good rate capability and cycling stability as used in MSIB.

2. Experimental section

2.1. Synthesis of NTP-NW/C and NTP-P/C

First, 1 mmol Titanium (IV) oxide acetylacetonate ($C_{10}H_{14}O_5Ti$) was slowly added into 20 mL iso-propyl alcohol and vigorously stirred for 1 h to obtain a pale-yellow solution. Then 0.18 mL H_3PO_4 was dropwise added into the above solution with continuous stirring until a uniform yellow suspension was obtained. After that, 1 mmol CH_3COONa (dissolved in 20 mL deionized water) was slowly added and the mixture was further stirred for 4 h to obtain a homogenous white colloidal solution. Then the obtained solution was transferred into a 50 mL Teflon-lined stainless-steel autoclave and kept at 180 °C for 12 h. When the reaction completed, the system was cooled to room temperature naturally. The white product was separated by centrifugation, washed with deionized water and ethanol for several times before drying at 70 °C overnight. Then 150 mg of white product and 100 mg of dopamine hydrochloride were dispersed into 100 mL of Tris-buffer solution (10 mM) with magnetic stirring for 4 h. The resultant gray product was collected via centrifugation and washed with deionized water and ethanol for three times, respectively, and dried at 70 °C overnight.

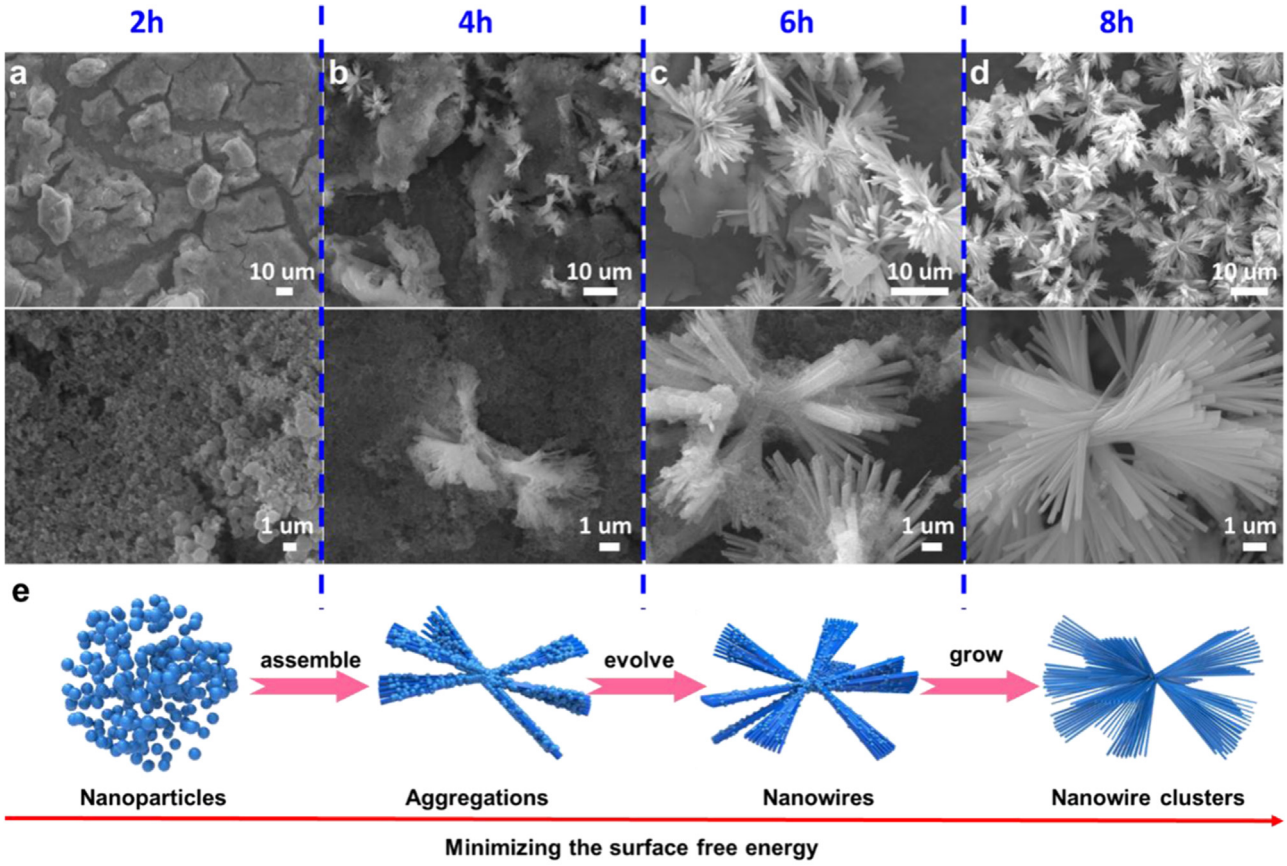

Fig. 2. The FESEM images (a–d) of NTP nanowire cluster precursors prepared by adjusting the solvothermal reaction time: (a) 2 h, (b) 4 h, (c) 6 h, (d) 8 h. (e) Schematic illustration of morphology evolution of the hierarchical nanowire cluster precursors.

Finally, NTP-NW/C was obtained by preheating the precursor at 400 °C for 2 h followed by annealing at 700 °C for 6 h in Ar with a heating rate of 2 °C min^{-1}. As control experiment, the precursors gained at a solvothermal treatment time of 2 h were also subjected through the same process. Finally the carbon-coated NTP particles (denoted as NTP-P/C) were obtained.

2.2. Material characterization

XRD (Burker D8 Advanced X-ray diffractometer with Cu-Kα radiation) was employed to obtain the crystallographic information of the two samples. Field emission scanning electron microscopy (FESEM) images were collected with a JEOL-7100F microscope at an acceleration voltage of 10 kV. Energy dispersive X-ray spectra (EDS) element mappings were recorded using an Oxford IE250 system. Transmission electron microscopy (TEM) and high resolution TEM (HRTEM) images were recorded by using a JEM-2100F STEM/EDS microscope. CHN elemental analyzer and thermo gravimetric analysis (TGA, STA-449C) were conducted in determining the carbon content of the NTP-NW/C. Raman spectra were obtained using a Renishaw INVIA micro-Raman spectroscopy system. Brurauer–Emmerr–Teller (BET) surface areas were measured using a Tristar II 3020 instrument by adsorption of nitrogen at 77 K. For in-situ XRD study, an electrochemical cell module with a beryllium window was used, while the slurry was directly cast on the beryllium window.

2.3. Measurement of electrochemical performance

The electrochemical measurements were carried out by assembling 2016 coin cells in a glove box filled with pure argon. In sodium half cells, sodium metal was used as the anode. The active electrode was made by putting the mixture of 70 wt% active materials, 20 wt% carbon black, and 10 wt% PVDF with an appropriate amount of N-methyl-2-pyrrolidone (NMP) as a solvent on a Cu foil. After drying at 70 °C for 12 h, the electrode was dried in a vacuum oven for 4 h at 100 °C. The electrolyte was composed of 1 M solution of $NaClO_4$ in propylene carbonate (PC) with 5% fluoroethylene carbonate (FEC). The glass fiber (GF/D) from Whatman was used as the separator. The galvanostatic discharge-charge tests of were carried out in a voltage window of 1.5–3.0 V on a battery test system (LAND CT2001A). The specific capacities were calculated based on the mass of NTP active material. For the Mg-based hybrid ion batteries (NTP-NW/C//Mg), the active electrode was made by putting the mixture of 70 wt% active materials, 20 wt% carbon black, and 10 wt% polytetrafluoroethylene (PTFE) binder. The active area of the electrode is about 0.8 cm^{-2}, and the mass loading of active material in electrodes is around 1.5 mg cm^{-2}. A typical of 20 mL 0.2 M $[Mg_2Cl_2][AlCl_4]_2$/DME electrolyte was prepared according to Doron Aurbach et al. [26] and Yan Yao et al. [12]. The hybrid-ion electrolyte was prepared by dissolving 0.4 M $NaAlCl_4$ (Alfa Aesar) into the above electrolyte. Magnesium metal was used as the anode, tainless steel was as the current collector, and glass fiber was used as the separator. The galvanostatic charge–discharge and GITT tests were carried out at a voltage window of 0.5–1.8 V on a battery test system (LAND CT2001A). AC-impedance spectra were tested at Autolab PGSTAT 302N with sweep frequency of 0.01–100000 Hz.

3. Results and discussion

The synthesis procedure of the NTP-NW/C is shown in Fig. S1 (Supporting information). Briefly, iso-propyl alcohol was selected as the dispersing agent to dissolve Titanium (IV) oxide acetylacetonate. A proper amount of H_3PO_4 and CH_3COONa aqueous solution were

sequentially dropped into the above solution to finally obtain a homogeneous white colloidal solution. Solvothermal treatment of the resulting solution at 180 °C for 12 h led to the formation of nanowires assembled 3D hierarchical microcluster precursors (Fig. S2, Supporting information). The length of the nanowires is ~10 μm, and the diameter is ~100 nm (Fig. S2a–c, Supporting information). The selected area electron diffraction pattern shows no obvious diffraction pattern, demonstrating the amorphous state of the precursors. HRTEM image (Fig. S2d, Supporting information) also verifies the same result. In order to elucidate the growth mechanism of the precursors, time-dependent experiments under solvothermal conditions were conducted. As shown in Fig. 2a, only primary nanoparticles with high surface energies could be clearly observed after a solvothermal treatment of 2 h. As the solvothermal reaction time increased to 4 h, the primary nanoparticles began to self-assemble into radial nanowires from the inside out due to the oriented attachment (Fig. 2b) [27]. To further reduce the surface energies, the length of nanowires grew gradually and the amount of nanowires increased further with the consumption of primary nanoparticles (Fig. 2c). As the solvothermal treatment increased to 8 h (Fig. 2d), microclusters assembled by nanowires were formed to minimize the overall surface energies [27,28]. Finally, hierarchical microclusters were entirely evolved as the solvothermal treatment extended to 12 h. The formation mechanism of hierarchical microcluster precursor is schematically illustrated in Fig. 2e. After coating with dopamine hydrochloride and annealing treatment, the 3D hierarchical NTP-NW/C was finally obtained. As control experiment, the precursors gained at a solvothermal treatment time of 2 h were also subjected through the same process. Finally the carbon-coated NTP particles (denoted as NTP-P/C) were obtained.

Fig. 3a shows the X-ray diffraction (XRD) pattern of the NTP-NW/C. All of the diffraction peaks are indexed to the rhombohedral NTP structure (JCPDS No. 01-085-2265), matching well with previous study [21–25]. The sharp and intense diffraction peaks suggest the well crystallized characteristic of NTP-NW/C. The detailed morphology and structure of NTP-NW/C were characterized by scanning electron microscopy (SEM) and transmission electron microscopy (TEM). SEM images (Fig. 3b, c) clearly display that the NTP-NW/C well inherits the hierarchical microcluster morphology of the precursors, and no obvious structure collapse is observed after annealing. The microclusters have an average diameter of ~10 μm, and are assembled by NTP nanowires which are radiated from the inside to outside. The TEM images (Fig. 3d,e) clearly show that the self-assembled NTP-NW/C nanosturctures consist of branched nanowires of ~5 μm length and ~100 nm diameter. The high-resolution TEM (HRTEM) image (Fig. 3f) displays lattice fringes with a d-spacing of 3.7 Å, corresponding to the (113) planes of the rhombohedral NTP. The thickness of carbon layer is determined to be 5 nm. XRD pattern of NTP-P/C (Fig. S3a, Supporting information) also manifests high purity and crystallinity, similar to that of NTP-NW/C. SEM, TEM and HRTEM images show that the NTP-P/C consists of irregular particles with amorphous carbon coating (Fig. S3b–f, Supporting information).

Determined from CHNS elemental analysis, the carbon contents of NTP-NW/C and NTP-P/C are 7.32 wt% and 7.59 wt%. TGA curve also confirms the low carbon content as shown in Fig. S4a. Furthermore, Raman spectra are used to identify the nature of carbon on the surface of NTP-NW/C and NTP-P/C (Fig. S4b, Supporting information). The D (derived from disordered carbon) and G (graphite carbon) bands of NTP-NW/C and NTP-P/C are observed at around 1342, 1610 and 1337, 1603 cm^{-1}, respectively. The intensity ratio of D band to G band (ID/IG) for NTP-NW/C is around 0.90, a bit larger than that of NTP-P/C (0.93), suggesting high graphitization degree and hence high electronic

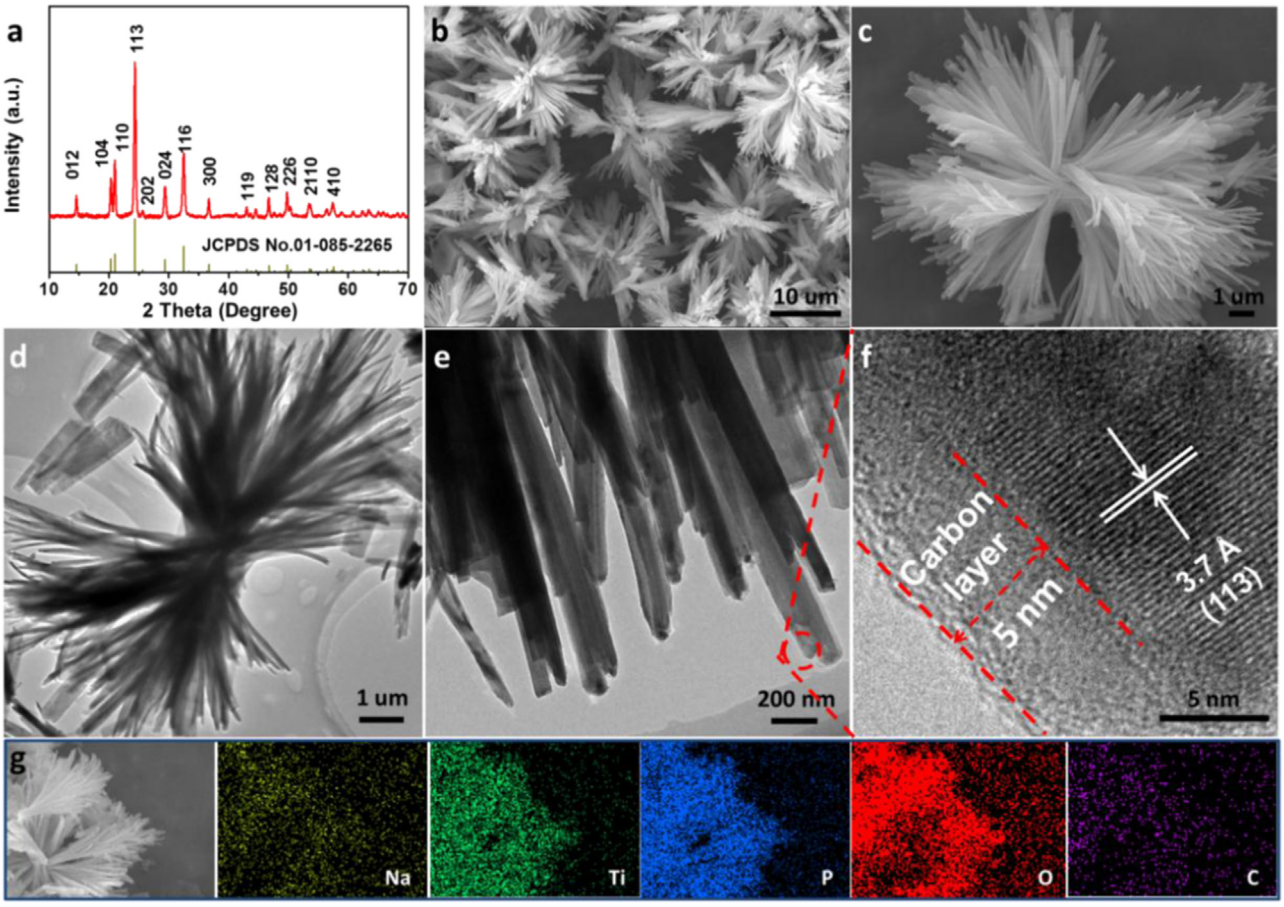

Fig. 3. (a) The XRD diffraction pattern, (b,c) FESEM images, (d,e) TEM images, (f) HRTEM image and (g) corresponding EDS elemental mappings of NTP-NW/C.

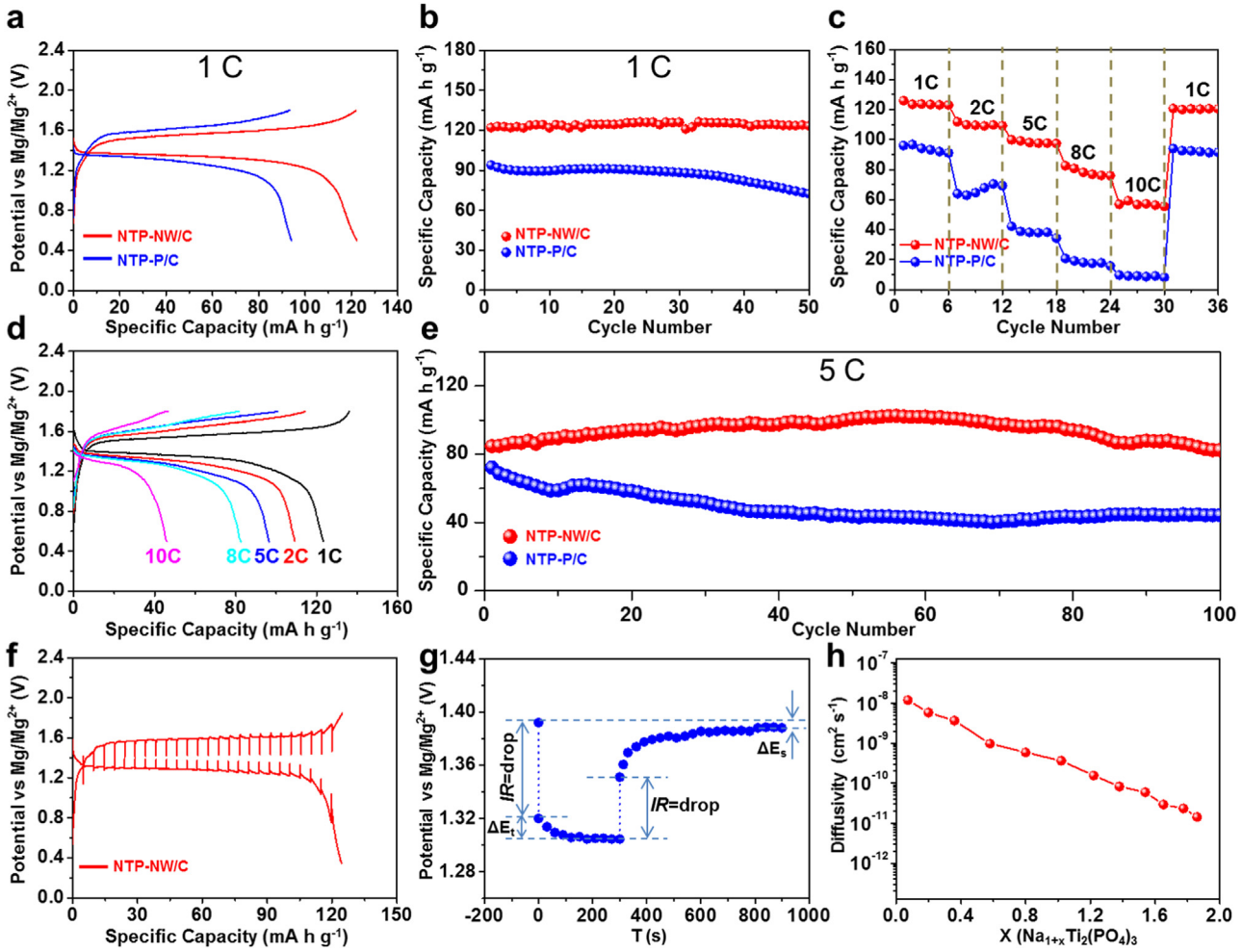

Fig. 4. (a) The discharge-charge curves of NTP-NW/C and NTP-P/C at 1 C between 0.5 and 1.8 V. (b) Cycling performances of NTP-NW/C and NTP-P/C at 1 C. (c) The rate performances of NTP-NW/C and NTP-P/C. (d) Discharge-charge curves of the NTP-NW/C at different rates. (e) Cycling performances of NTP-NW/C and NTP-P/C at 5 C. (f) GITT curve of NTP-NW/C at 0.5–1.8 V. (g) GITT potential response curve with time. The experiment was carried out at constant current pulse of 50 mA g^{-1} for 5 min followed by a relaxation period of 10 min and avoltage range.(h) Diffusivity versus state of discharge.

conductivity [20]. The BET surface area of NTP-NW/C and NTP-P/C were measured to be 79.50 and 42.76 m^2 g^{-1}, respectively (Fig. S5, Supporting information). The much higher surface area of NTP-NW/C would facilitate electrolyte penetration and enhance effective contact between electrolyte and electrode [29].

Before the study of electrochemical properties for MSIB. We assembled Na-ion half cells to explore the sodium storage properties of the two samples. As shown in Fig. S6, the NTP-NW/C exhibits remarkable sodium storage performance. Further investigations of the electrochemical performances for the prepared samples were carried out by the assembly of full-cells (2016-type coin cell) with magnesium metal as anode, 0.2 M $[Mg_2(m\text{-}Cl)_2][AlCl_4]_2$ + 0.4 M $NaAlCl_4$ in DME as the electrolyte and stainless steel as the current collector. Fig. S7 shows the electrochemical performance of the hybrid electrolyte via cyclic voltammetry (CV) using a three-electrode setup. The current response shows good reversibility for Mg deposition and dissolution in different cycles [12,20]. The coulombic efficiency calculated from the voltammetric current for each dissolution/deposition cycle was increased from 90% (1st cycle) to 98% (50th cycle). Fig. 4a shows the galvanostatic voltage profiles of NTP-NW/C and NTP-P/C in the hybrid electrolyte with a voltage window of 0.5–1.8 V at 1 C (1 C = 133 mA g^{-1}). Both the samples exhibit two platforms at around 1.4 V (*vs* Mg/Mg^{2+}). But the NTP-NW/C delivers smaller overpotential of 169 mV and higher capacity of 124 mA h g^{-1} (close to the theoretical capacity) compared to that of the NTP-P/C (270 mV and 92 mA h g^{-1}). Both the capacities are based on the mass of total NTP/C. The smaller polarization of the former could be attributed that the primary 1D nanowires reduce the diffusion length for Na^+ and uniform carbon-coating improves electronic conductivity. After 50 cycles (Fig. 4b), the capacity retention is almost 100%, which shows better cycle stability compared with that of NTP-P/C (77%) at low current density. Moreover, the cycling performances of NTP-NW/C at 0.5 C with different concentration of $NaAlCl_4$ (0.1, 0.2, 0.3, and 0.4 M) were performed to investigate the influence of $NaAlCl_4$ concentration on the electrochemical performance of the NTP-NW/C (Fig. S8). Here, the 0.4 M is the highest concentration can be achieved. Obviously, with the increase of concentration of $NaAlCl_4$, the NTP-NW/C exhibits a better electrochemistry performance. This is because the amount of Na^+ is insufficient for inserting into the cathode at low concentrations. Even though increased concentration results in the raised viscosity and low conductivity, the more Na-ions can meet the needs for the cathode, and the effect of the increased Na^+ transference number counteracts the effect of low conductivity. So, when the $NaAlCl_4$ concentration is up to the highest concentration of 0.4 M, the electrochemistry performance is obviously superior to other systems. The rate performance and corresponding charge/discharge curves of the NTP-NW/C and NTP-P/C are shown in Fig. 4c, d and Fig. S9. Clearly, the rate performance of NTP-NW/C is much better than that of NTP-P/C. For NTP-NW/C, it delivers a high capacity of 125 mA h g^{-1} at a low discharge rate of 1 C. As the discharge rates increase to 10 C, the reversible capacities can remain

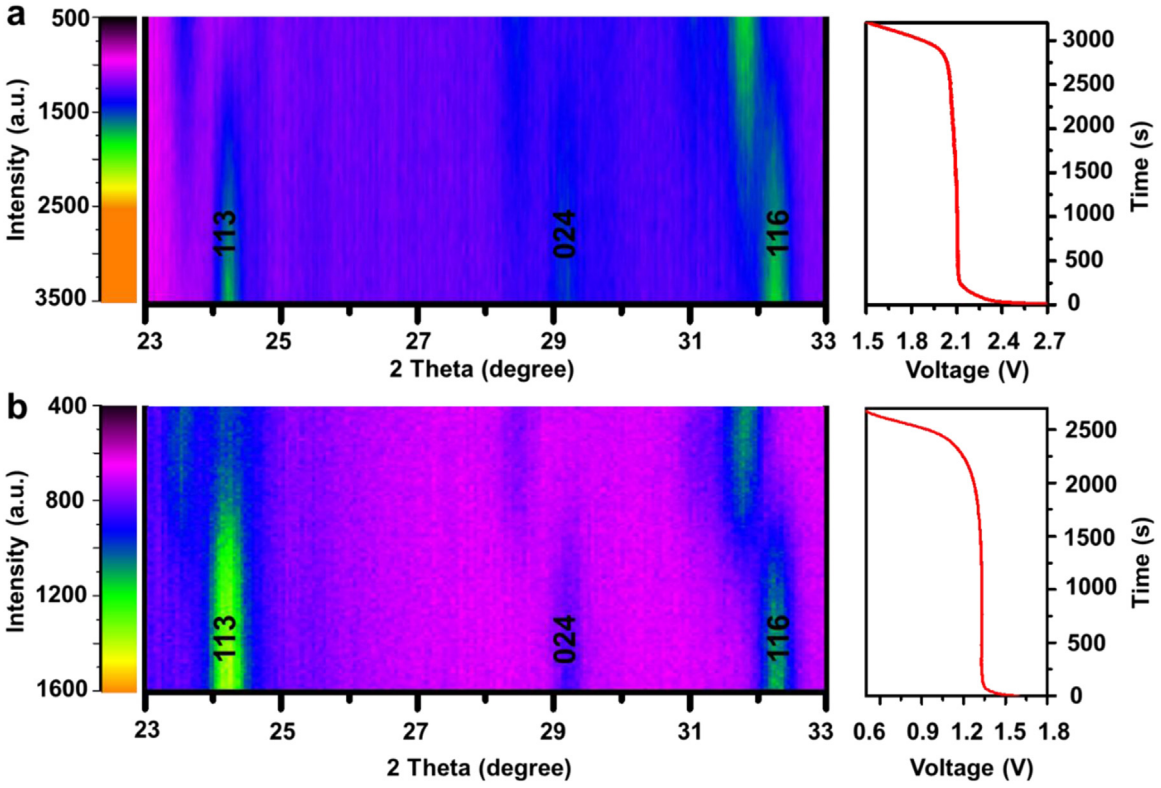

Fig. 5. *In-situ* XRD patterns of NTP-NW/C in different battery systems: (a) the image plot of diffraction patterns in Na-ion half cell during the discharge process at 1 C and a voltage range of 1.5–3.0 V; (b) the image plot of diffraction patterns in Mg-Na hybrid battery systems during the discharge process at 1 C and a voltage range of 0.5–1.8 V.

60 mA h g^{-1}. When the rate is turned back to 1 C, it shows good capacity recoverability. From the discharge-charge curves of NTP-NW/C at different rates, the voltage plateaus are still distinct even at a high rate of 10 C, which fully proves the high carrier mobility in NTP-NW/C. But for the NTP-P/C, high polarization and no obvious discharge-charge plateaus can be observed above 5 C (Fig. S9). Fig. 4e shows the cycling performance of the two samples at a high discharge rate of 5 C. Compared with NTP-P/C, the NTP-NW/C delivers higher initial specific capacity of 85 mA h g^{-1} and more stable cycling life (the capacity retention is up to 97% after 100 cycles). It is worth noting that like the previous reports [10,12,20], much longer cycle life (more than several hundred cycles) is still a bottleneck faced by the Mg-Na hybrid battery systems at present. This may be due to the following two reasons. Firstly, due to the complex electrolyte systems, in addition to the redox reactions at the cathode and anode, there may be side reactions between the electrolytes that hinder ions migration as the reaction progresses. Secondly, in the high charging voltage areas, side reaction between the current collector and electrolyte produces passive film, which will increase the internal resistance of the battery, resulting in capacity loss and lower discharge efficiency. Therefore, developing more stable and efficient electrolyte will be the key to improve the cycle life. The morphology features of NTP-NW/C after 100 cycles at 5 C are shown in Fig. S10. Obviously, the 3D open architecture assembled by radial nanowires is well maintained, indicating the robust structural stability during long term cycling. The surface morphologies of the Mg anode before and after 100 cycles at 5 C were also examined under SEM (Fig. S11). The results display that no dendrites growth on Mg deposition.

The electrochemical impedance spectra (EIS) measurements on the assembled cells under different conditions were investigated to reveal the reason for the enhanced electrochemical performance for the 3D hierarchical microclusters. The Nyquist plots of the two samples are shown in Fig. S12. After the first charge and discharge activation at 5 C, the charge transfer resistance (Rct) of the NTP-NW/C is determined to be 120 Ω, which is smaller than that of NTP-P/C (200 Ω), suggesting the improved charge transfer kinetics. Besides, compared with that of NTP-P/C, the Rct of NTP-NW/C changes slightly after 100 cycles at 5 C, indicating that the 3D hierarchical structure and uniform dispersion of carbon skeleton provide efficient ion/electron transport upon cycling [30,31]. Galvanostatic intermittent titration technique (GITT) of NTP-NW/C is performed as shown in Fig. 4f to further investigate the kinetics of ion solid-state diffusion. The NTP-NW/C delivers a specific capacity of 124 mA h g^{-1} in the voltage window of 0.5–1.8 V, corresponding to a discharge product of $Na_{1+x}Ti_2(PO_4)_3$ (x = 1.86). In addition, the diffusion coefficient D^{GITT} (cm^2 s^{-1}) can be calculated according to the following formula (1) [8,32]:

$$D^{GITT} = \frac{4}{\pi\tau}\left(\frac{m_B V_M}{M_B S}\right)^2\left(\frac{\Delta E_s}{\Delta E_\tau}\right)^2 \quad (1)$$

where τ, m_B, V_M, M_B and S are the constant current pulse time, mass, molar volume, molar mass, and electrode–electrolyte interface area of NTP-NW/C, respectively. ΔE_s is the voltage difference during the open circuit period, and ΔE_t represents the total change of cell voltage during a constant current pulse excluding the *IR* drop (Fig. 4g). The calculated diffusion coefficients of NTP-NW/C and NTP-P/C are shown in Fig. 4f and Fig. S13. From the calculation results, even the Na diffusivity of NTP-NW/C decreases from 1.2×10^{-8} to 1.4×10^{-11} cm^2 s^{-1} due to the charge repulsion resulting from Na concentration increases in the host, the average diffusion coefficient of NTP-NW/C is much higher than that of NTP-P/C, which evidently proves the fast charge transfer kinetics and thus the enhanced electrochemical performance.

In order to investigate the charge storage behavior of the hybrid battery system, the electrochemical performance of NTP-NW/C was performed in the pure Mg electrolyte without $NaAlCl_4$. As shown in Fig. S14 (Supporting information), the NTP-NW/C almost does not provide reversible capacity even after 100 cycles' activation, demonstrating that

Mg^{2+} does not insert into the NTP-NW/C host in this system. In addition, time-resolved in-situ XRD techniques further demonstrate this result. Both in the Na-ion half-cell system (Fig. 5a) and the hybrid battery system (Fig. 5b), clear and identical variations are observed in the ion intercalation process at 1 C. The peaks centered at 24.2°, 29.2°, and 32.3°, corresponding to the (113), (024), and (116) diffractions of NTP-NW/C, disappear eventually along with the appearance and gradual enhancement of new diffractions at 23.5°, 28.4°, and 31.8°, revealing the formation of new phase $Na_3Ti_2(PO_4)_3$ after the first complete discharge in both the systems [33,34]. These results fully prove the sodium intercalation phase transformation process of NTP in both the two systems. Therefore, during the discharge process for this hybrid battery system, Na^+ is inserted into NTP framework at the cathode side, and simultaneously metallic Mg anode may reacts with $AlCl_4^-$ to form $[Mg_2Cl_2]^{2+}$ due to that $AlCl_4^-$ is easier than $MgCl^+$ to lose Cl^- [12,20,35]. The detailed reaction can be summaried as follows:

$$\text{Cathode: } NaTi_2(PO_4)_3 + 2Na^+ + 2e^- \leftrightarrow Na_3Ti_2(PO_4)_3 \quad (2)$$

$$\text{Anode: } Mg + AlCl_4^- \leftrightarrow 1/2[Mg_2Cl_2]^{2+} + AlCl_3 + 2e^- \quad (3)$$

$$\text{Overall: } NaTi_2(PO_4)_3 + 2NaAlCl_4 + Mg \leftrightarrow Na_3Ti_2(PO_4)_3 + 1/2[Mg_2Cl_2][AlCl_4]_2 + AlCl_3 \quad (4)$$

Based on the above results, it is evident that the capacity contribution is completely determined by the Na^+ intercalation/deintercalation in this hybrid battery system.

4. Conclusion

In summary, a high-performance MSIB using NASICON-type NTP-NW/C nanowire clusters as the cathode and dendrite-free Mg metal as the anode has been successfully assembled. Combining the advantages of NTP nanowires and the homogeneous carbon skeleton, the novel 3D hierarchical structure offers short Na^+ transport pathway, rapid charge transfer speed and stable structure during sodiation/de-sodiation. Together with these nanoarchitecture features, as in our results, the electrochemical performances of the hybrid MSIB systems are impressive: a high reversible capacity of 124 mA h g^{-1} at 1 C, good rate capability (60 mA h g^{-1} at 10 C) and long cycle life with capacity retention of 97% after 100 cycles at 5 C. Our work demonstrates that the novel 3D hierarchical NTP-NW/C is a very promising electrode for the high performance MSIBs. We believe that this novel strategy may discover further possibilities to develop large scale energy storage applications.

Acknowledgements

This work was supported by the National Key Research and Development Program of China (2016YFA0202603, 2016YFA0202601), the National Natural Science Fund for Distinguished Young Scholars (51425204), the National Natural Science Foundation of China (51521001, 51602239), the Programme of Introducing Talents of Discipline to Universities (B17034), the Hubei Provincial Natural Science Foundation of China (2016CFB267), the Yellow Crane Talent (Science & Technology) Program of Wuhan City, the International Science & Technology Cooperation Program of China (2013DFA50840) and the Fundamental Research Funds for the Central Universities (WUT: 2017III009, 2017III005).

Appendix A. Supporting information

Supplementary data associated with this article can be found in the online version at doi:10.1016/j.nanoen.2018.10.064.

References

[1] J.W. Choi, D. Aurbach, Nat. Rev. Mater. 1 (2016) 16013.
[2] H.D. Yoo, I. Shterenberg, Y. Gofer, G. Gershinsky, N. Pour, D. Aurbach, Energy Environ. Sci. 6 (2013) 2265–2279.
[3] P. Saha, M.K. Datta, O.I. Velikokhatnyi, A. Manivannan, D. Alman, P.N. Kumta, Prog. Mater. Sci. 66 (2014) 1–86.
[4] Y. Cheng, Y. Shao, L.R. Parent, M.L. Sushko, G. Li, P.V. Sushko, N.D. Browning, C. Wang, J. Liu, Adv. Mater. 27 (2015) 6598–6605.
[5] J. Muldoon, C.B. Bucur, T. Gregory, Chem. Rev. 114 (2014) 11683–11720.
[6] W. Kaveevivitchai, A.J. Jacobson, Chem. Mater. 28 (2016) 4593–4601.
[7] L. Wang, K. Asheim, P.E. Vullum, A.M. Svensson, F. Vullumbruer, Chem. Mater. 28 (2016) 6459–6470.
[8] Q. An, Y. Li, H.D. Yoo, S. Chen, Q. Ru, L. Mai, Y. Yao, Nano Energy 18 (2015) 265–272.
[9] D. Aurbach, Z. Lu, A. Schechter, Y. Gofer, H. Gizbar, R. Turgeman, Y. Cohen, M. Moshkovich, E. Levi, Nature 407 (2000) 724–727.
[10] M. Walter, K.V. Kravchyk, M. Ibáñez, M.V. Kovalenko, Chem. Mater. 27 (2015) 7452–7458.
[11] J.L. Andrews, A. Mukherjee, H.D. Yoo, A. Parija, P.M. Marley, S. Fakra, D. Prendergast, J. Cabana, R.F. Klie, S. Banerjee, Chem 4 (2018) 1–22.
[12] H. Dong, Y. Li, Y. Liang, G. Li, C.J. Sun, Y. Ren, Y.H. Lu, Y. Yao, Chem. Commun. 52 (2016) 8263–8266.
[13] X. Sun, P. Bonnick, V. Duffort, M. Liu, Z. Rong, K.A. Persson, G. Ceder, L.F. Nazar, Energy Environ. Sci. 9 (2016) 2273–2277.
[14] K. Lu, B. Song, J. Zhang, H. M, J. Power Sources 321 (2016) 257–263.
[15] T. Gao, F. Han, Y. Zhu, L. Suo, C. Luo, K. Xu, C. Wang, Adv. Energy Mater. 5 (2015) 1401507.
[16] H.D. Yoo, Y. Liang, Y. Li, Y. Yao, ACS Appl. Mater. Interfaces 7 (2015) 7001–7007.
[17] Y. Cheng, Y. Shao, J.G. Zhang, V.L. Sprenkle, J. Liu, G. Li, Chem. Commun. 50 (2014) 9644–9646.
[18] S. Su, Y. NuLi, Z. Huang, Q. Miao, J. Yang, J. Wang, ACS Appl. Mater. Interfaces 8 (2016) 7111–7117.
[19] Y. Xu, C. Xu, Q. An, Q. Wei, J. Sheng, F. Xiong, C. Pei, L. Mai, J. Mater. Chem. A 5 (2017) 13950–13956.
[20] Y. Li, Q. An, Y. Cheng, Y. Liang, Y. Ren, C.-J. Sun, H. Dong, Z. Tang, G. Li, Y. Yao, Nano Energy 34 (2017) 188–194.
[21] Y. Fang, L. Xiao, J. Qian, Y. Cao, X. Ai, Y. Huang, H. Yang, Adv. Energy Mater. 6 (2016) 1502197.
[22] C. Wu, P. Kopold, Y.L. Ding, P.A.V. Aken, J. Maier, Y. Yu, ACS Nano 9 (2015) 6610–6618.
[23] W. Wu, J. Yan, A. Wise, A. Rutt, J. Whitacre, J. Electrochem. Soc. 161 (2014) A561–A567.
[24] H.K. Roh, H.K. Kim, M.S. Kim, D.H. Kim, K.Y. Chung, K.C. Roh, K.B. Kim, Nano Res. 9 (2016) 1844–1855.
[25] C. Xu, Y. Xu, C. Tang, Q. Wei, J. Meng, L. Huang, L. Zhou, G. Zhang, L. He, L. Mai, Nano Energy 28 (2016) 224–231.
[26] R.E. Doe, R. Han, J. Hwang, A.J. Gmitter, I. Shterenberg, H.D. Yoo, N. Pourb, D. Aurbach, Chem. Commun. 50 (2014) 243–245.
[27] Y. Li, J. Liu, X. Huang, G. Li, Cryst. Growth Des. 7 (2007) 1350–1355.
[28] A.Q. Pan, H.B. Wu, L. Zhang, X.W.D. Lou, Energy Environ. Sci. 6 (2013) 1476–1479.
[29] Y. Jiang, Z. Yang, W. Li, L. Zeng, F. Pan, M. Wang, X. Wei, G. Hu, L. Gu, Y. Yu, Adv. Energy Mater. 5 (2015) 1402104.
[30] X. Wang, X. Xu, C. Niu, J. Meng, M. Huang, X. Liu, Z. Liu, L. Mai, Nano Lett. 17 (2017) 544–550.
[31] X. Wang, C. Niu, J. Meng, P. Hu, X. Xu, X. Wei, L. Zhou, K. Zhao, W. Luo, M. Yan, L. Mai, Adv. Energy Mater. 5 (2015) 1500716.
[32] C. Pei, F. Xiong, J. Sheng, Y. Yin, S. Tan, D. Wang, C. Han, Q. An, L. Mai, ACS Appl. Mater. Interfaces 9 (2017) 17060–17066.
[33] P. Senguttuvan, G. Rousse, M. Arroyo y de Dompablo, H. Vezin, J.-M. Tarascon, M. Palacín, J. Am. Chem. Soc. 135 (2013) 3897–3903.
[34] Z. Li, D.B. Ravnsbæk, K. Xiang, Y.-M. Chiang, Electrochem. Commun. 44 (2014) 12–15.
[35] P. Canepa, S. Jayaraman, L. Cheng, N.N. Rajput, W.D. Richards, G.S. Gautam, L.A. Curtiss, K.A. Perssond, G. Ceder, Energy Environ. Sci. 8 (2015) 3718–3730.

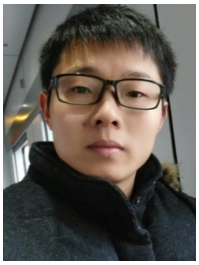

Yanan Xu received his B.S. degree in Department of Materials Science of Engineering from Wuhan University of Technology in 2013. He is currently working toward the Ph.D. degree. His current research involves the nanomaterials achieving high energy density and power density for lithium ion battery, sodium ion battery and magnesium ion battery.

Weijie Cao is an undergraduate student from the School of Materials Science and Engineering at Wuhan University of Technology (WUT) since 2015. He has joined the tutorial system of undergraduates at the WUT Nano Key Laboratory and studies in Mai Research Group. His current research focuses on energy storage materials and devices.

Yameng Yin received her B.S. degree in Department of Materials Science and Engineering from Hebei University of Architecture in 2014. She is currently working toward the Ph.D. degree and her current research focuses on electrode materials for emerging energy storage devices.

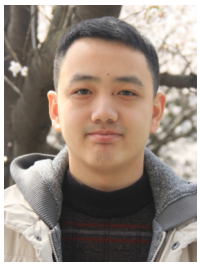

Jinzhi Sheng received his M.S. degree in Materials Engineering from Wuhan University of Technology in 2015. He is currently working toward the Ph.D. degree and his current research focuses on the energy storage materials and devices.

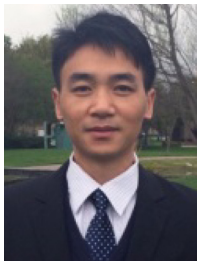

Qinyou An is Associate Professor of Materials Science and Engineering at Wuhan University of Technology (WUT). He received his Ph.D. degree from WUT in 2014. He carried out his postdoctoral research in the laboratory of Prof. Yan Yao at the University of Houston in 2014–2015. Currently, his research interest include energy storage materials and devices.

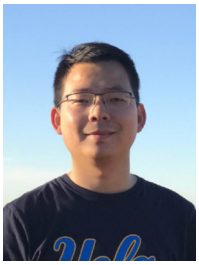

Qiulong Wei received his Ph.D. from the State Key Laboratory of Advanced Technology for Materials Synthesis and Processing, Wuhan University of Technology in 2016, under the supervision of Prof. Qingjie Zhang and Prof. Liqiang Mai. Currently, he is a postdoctoral fellow in the laboratory of Prof. Bruce Dunn at the Materials Science and Engineering, UCLA. His current research involves the design and control the electrode-electrolyte interface for achieving high-rate electrochemical energy storage devices.

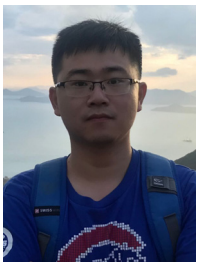

Wei Yang received his Master's degree in Materials Engineering from Wuhan University of Technology in 2017. He was a research assistant at Wuhan University of Technology from 2017 to 2018. He is currently working toward the Ph.D. degree and his research interests focus on micro energy storage devices.

Liqiang Mai is Chair Professor of Materials Science and Engineering at Wuhan University of Technology (WUT). He is Cheung Kong Scholar Chair Professor and the winner of the National Natural Science Fund for Distinguished Young Scholars. His current research interests focus on new nanomaterials for electrochemical energy storage and micro/nano energy devices. He received his Ph.D. degree from WUT in 2004. He carried out his postdoctoral research in the laboratory of Prof. Zhonglin Wang at Georgia Institute of Technology in 2006–2007 and worked as advanced research scholar in the laboratory of Prof. Charles M. Lieber at Harvard University in 2008–2011. He worked as advanced research scholar in the laboratory of Prof. Peidong Yang at University of California, Berkeley in 2017.